Insight into the Dynamic Recrystallization Behavior and Microstructure Evolution of MP159 Superalloy During Hot Deformation

Yeqing Cai[1] · Song Xiang[1] · Yuanbiao Tan[1]

Abstract

The dynamic recrystallization behavior of MP159 superalloy was investigated by performing hot compression tests in the deformation temperature range of 920–1070 °C and strain rates of 0.01–10 s^{-1}. Processing maps were established based on flow curves, and the optimal hot processing region for MP159 alloy was identified at the deformation temperatures of 940–980 °C and a strain rate of 0.01 s^{-1}. The influence of the processing parameters (true strain, temperature and strain rate) on the microstructure evolution was studied. The volume fraction and grain size of recrystallized grains increased with increasing strain rate and deformation temperature. Deformation twins that formed during hot deformation provided nucleation sites for dynamic recrystallization (DRX) and accelerated the DRX process. Discontinuous dynamic recrystallization (DDRX) was the dominant mechanism for the MP159 alloy at different deformation strains.

Keywords MP159 superalloy · Hot deformation · Processing map · Microstructure evolution · Dynamic recrystallization mechanism

1 Introduction

MP159 alloy is a cobalt-based superalloy, which possesses a good combination property of ultrahigh strength, ductility and corrosion resistance [1]. Due to its superior mechanical properties, MP159 alloy is usually used for critical fasteners and prosthetic devices. Critical parts made of superalloys are commonly processed by hot deformation processes, such as hot forging and hot rolling [2]. The mechanical properties of the parts depend on the microstructure obtained from hot deformation. The microstructure evolution of the superalloy during hot deformation is a complex process, involving deformation heat, flow location, dynamic recovery and dynamic recrystallization. The size and volume fraction of recrystallized grains were significantly affected by hot-working parameters [3, 4]. Moreover, abnormal deformation conditions induce defects such as surface cracks and inhomogeneous grain size distributions. To fabricate critical parts with excellent mechanical properties, it is important to understand the hot deformation behavior and microstructure evolution of MP159 superalloy under different deformation conditions.

Recent studies have focused on the hot deformation behavior and microstructure evolution of various superalloys. Wu et al. [5] reported that the dynamic recrystallization of GH984G was strongly affected by the initial grain sizes of alloys. The dynamic recrystallization (DRX) mechanism for GH984G alloys is mainly continuous dynamic recrystallization (CDRX) for larger initial grains and discontinuous dynamic recrystallization (DDRX) for fine grains. Godasu et al. [6] observed the hot deformation of cast superalloy 625 and found that the dynamic recovery and DDRX mechanisms are mostly responsible for microstructural modification, and the formation of twins controlled the recrystallization rate. Moreover, factors including the initial δ phase, deformation temperature and strain rate also have a clear influence on the DRX of superalloys [7, 8]. Wen et al. [7] showed that the δ phase pre-existing in alloys first stimulates the occurrence of DRX and then gives rise to a weak effect with increasing deformation temperature. Lin et al. [8] pointed out that CDRX and DDRX occur at low deformation

✉ Song Xiang
sxiang@gzu.edu.cn

1 Guizhou Key Laboratory of Materials Mechanical Behavior and Microstructure, College of Materials and Metallurgy, Guizhou University, Guiyang 550025, People's Republic of China

and high deformation temperatures for a powder metallurgical nickel-based superalloy.

Above all, the hot deformation behavior of different superalloys varies with the chemical composition, initial grain size, initial phases, strain rate and deformation temperature. The MP159 superalloy is a Co–Ni–Cr-based multiphase superalloy and is usually applied in aerospace as a bolting workpiece produced by hot upset processes [9]. To achieve a uniform and fine microstructure in practical bolt manufacturing, the aim of this work was to better understand the hot deformation behavior and microstructure evolution of the MP159 superalloy during hot processing, and provide guidance for the selection of thermal deformation parameters in industrial production. A constitutive model based on the classical Arrhenius equation was established, and the processing maps and microstructure evolution were analyzed by systematic electron backscatter diffraction (EBSD) and transmission electron microscopy (TEM) analysis.

2 Experimental Procedure

The materials used in the study are commercial cold drawn MP159 rods. The chemical composition of the MP159 superalloy was 35.7Co-25.5Ni-19Cr-9Fe-7Mo-3Ti-0.6Nb-0.2Al wt %. In this work, the tests of hot deformation were carried out using a Gleeble 3800 thermomechanical simulator. Cylindrical specimens ($\Phi 8 \times 12$ mm) were prepared for hot compression. A schematic depiction of the hot deformation process was presented in Fig. 1. The specimens were heated at a rate of 10 °C/s to 920, 950, 980, 1010, 1040 and 1070 °C and were held for 2 min, respectively. The test was stopped after compressive deformation reached a true strain of 1.3 with strain rates of 0.01, 0.1, 1 and 10 s^{-1}, and then, the specimens were water quenched immediately inside the chamber to retain the deformation microstructure. The true

Fig. 1 Schematic depiction of the hot deformation process

stress–strain curves were plotted based on the data obtained by the compression tests.

For optical microstructural observation, the specimens were cut along the deformed compression axis. The specimens were mechanically ground using a series of abrasive papers of 180–3000 grit and subsequent diamond polishing. The polished surfaces were etched with aqua regia for 30 s. The microstructures were observed on the central part of the specimens using an Olympus GX51 instrument. The effects of different deformation conditions on the microstructures were evaluated using a TESCAN MIRA3 field-emission gun scanning electron microscope system, equipped with an Oxford Instrument HKL Nordlys Max3 EBSD detector. The specimens used for EBSD evaluation were mechanically ground and diamond polished, and then polished by vibrating with a 0.05 μm colloidal silica solution for 12 h. The EBSD maps were observed in the central part of the polished specimen with an accelerating voltage of 20 kV and a step size of 0.12 μm. HKL channel 5 software was used to acquire and analyze the EBSD data. For TEM observations, the specimens were first prepared by hand grinding to a thickness of 200 μm, and then the thinned specimens were punched out to holes with a diameter of 3 mm. Finally, the obtained specimens were ion milled to a thin foil with the Gatan 695 ion beam thinner. An FEI Talos F200X transmission electron microscopy (TEM) system operated at 200 kV was used for TEM measurements.

3 Results and Discussion

3.1 True Stress–Strain Curves

The true stress–strain curves at different deformation strain rates and temperatures are presented in Fig. 2. Generally, the variation in true stress is caused by work hardening and dynamic softening [10]. In the early deformation stage, the increase in the stress was due to strain hardening that was predominantly caused by dislocation multiplication and stacking. Meanwhile, due to the low stacking fault energy (SFE) of this superalloy, weak dynamic softening was induced by dislocation climb and annihilation. Consequently, the stress rapidly increased to a critical value. With the true strain increased, the true stress decreased due to the occurrence of DRX. The nucleation and growth of new dislocation-free grains by the annihilation of dislocations, led to a decrease in the work hardening rate and material softening. The appearance of the steady-state value was related to the dynamic balance between strain hardening and strain softening. In addition, it was observed that deformation parameters strongly affect the peak stress. It can be observed from Fig. 2 that the peak stress decreased with increasing deformation temperature. This was attributed
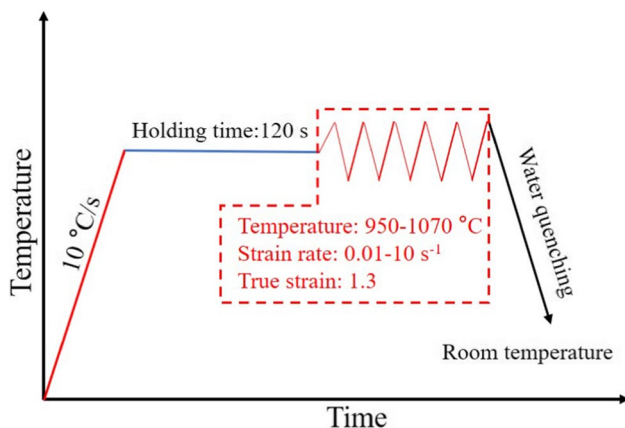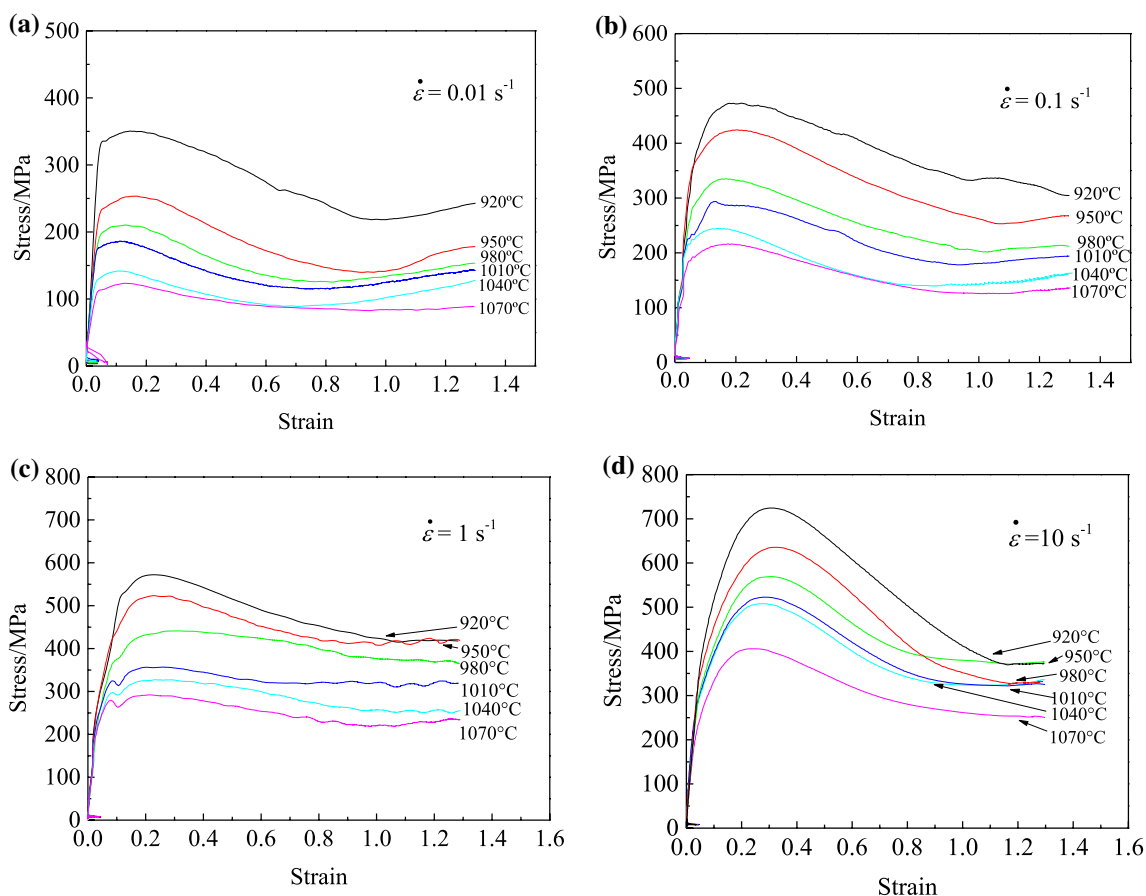
Fig. 2 The true stress–strain curves at different deformation strain rates and temperatures

to the decreased atomic binding force and increased solute atom motion with increasing temperature, which promote dislocation slip and grain boundary motion. Furthermore, the peak stress increased with increasing strain rate. Main reason is that the rate of dislocation generation and motion increased with increasing strain rate, which results in an increase in the degree of work hardening [11].

3.2 Constitutive Equation

The relationship between the flow stress, strain rate and temperature during the deformation process can be described by the classic Arrhenius constitutive equations given by [12]

$$\dot{\varepsilon} = A_1 \sigma^{n_1} \exp(-Q/RT), \qquad \alpha\sigma < 0.8 \tag{1}$$

$$\dot{\varepsilon} = A_2 \exp(\beta\sigma) \exp(-Q/RT), \qquad \alpha\sigma > 1.2 \tag{2}$$

$$\dot{\varepsilon} = A[\sinh(\alpha\sigma)]^n \exp(-Q/RT), \qquad \text{for all } \sigma \tag{3}$$

where $\dot{\varepsilon}$ is the strain rate (s^{-1}), σ is the flow stress (MPa) at a specific true strain, Q is the deformation activation energy

(kJ/mol), R is the universal gas constant (8.314 J/mol K), T is the deformation temperature (K), n and n_1 are the stress exponents, and A, A_1, A_2, α and β are material constants. The power-law equation in Eq. (1) is applicable for low stress, and the exponential law is suitable for high stress values (Eq. 2). The hyperbolic sine law in Eq. (3) is applicable to all stress levels, and therefore, it is more commonly used to describe the hot deformation constitutive relationship.
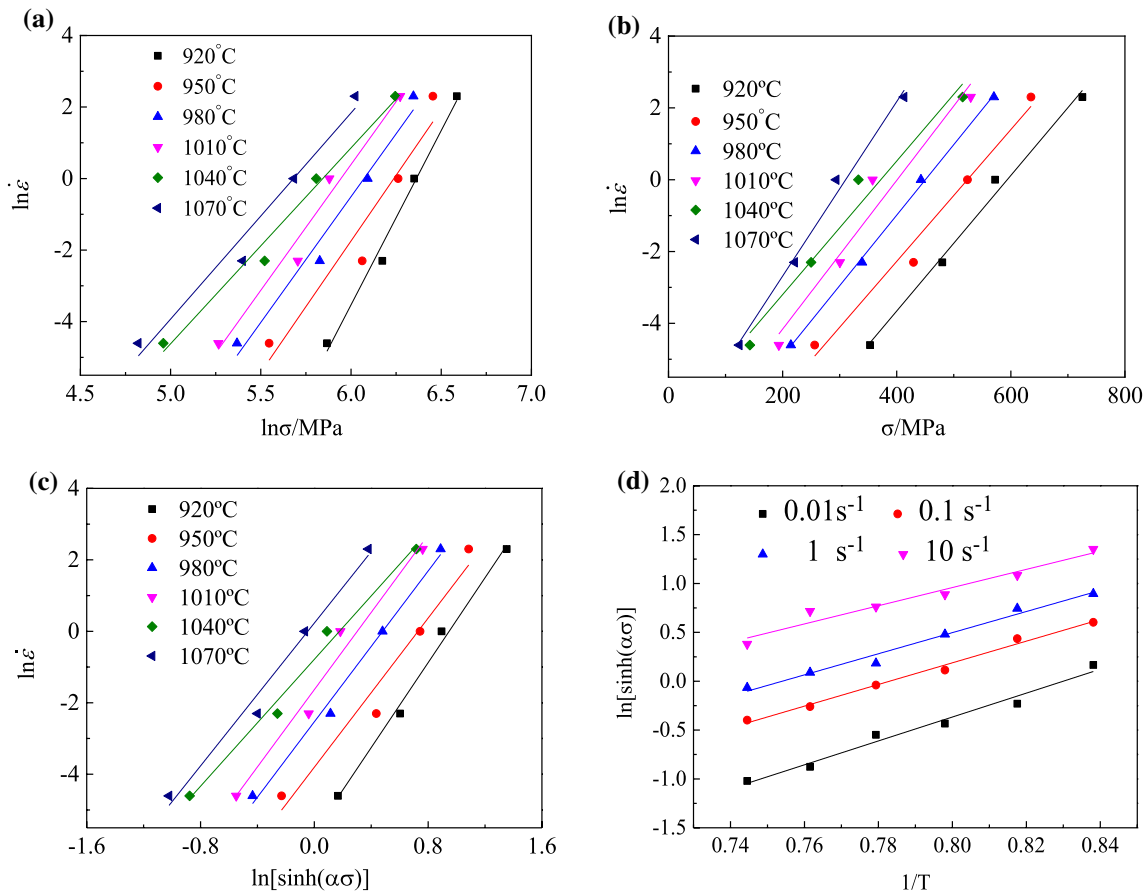
Taking the logarithm of both sides of Eqs. (1) and (2) gives

$$\ln\dot{\varepsilon} = \ln A_2 + \beta\sigma - Q/RT \tag{4}$$

$$\ln\dot{\varepsilon} = \ln A_2 + \beta\sigma - Q/RT \tag{5}$$

By partial differentiation at constant temperature T, the values of n_1 and β can be calculated.

Figure 3a and b show linear regression fits of the ln $\dot{\varepsilon}$ -lnσ and ln $\dot{\varepsilon}$-σ plots at different temperatures with mean slope values of 7.06593 and 0.02008 specifying n_1 and β, respectively. Since α is equal to β/n_1, it was estimated as 0.0028.

Fig. 3 plots of linear correlation **a** ln $\dot{\varepsilon}$-ln σ, **b** $\dot{\varepsilon}$-σ, **c** ln[sinh($\alpha\sigma$)]-ln $\dot{\varepsilon}$ and **d** ln[sinh($\alpha\sigma$)]-1/T

Taking the natural logarithms of both sides of Eq. (3) gives

$$\ln \dot{\varepsilon} = \ln A + n \ln \sinh(\alpha\sigma) - Q/RT \qquad (6)$$

Figure 3c shows the linear fit of the ln[sinh($\alpha\sigma$)]-ln $\dot{\varepsilon}$ plots obtained at various deformation temperatures. The average slope of the fitted line is *n* and was calculated to be 5.2129. By differentiating Eq. (6), the activation energy *Q* can be described as

$$Q = R \left\{ \frac{\partial \ln \dot{\varepsilon}}{\partial \ln[\sinh(\alpha\sigma)]} \right\} \left\{ \frac{\partial \ln[\sinh(\alpha\sigma)]}{\partial(1/T)} \right\}_{\dot{\varepsilon}} \qquad (7)$$

The linear fitting of the ln[sinh($\alpha\sigma$)]-1/T plot is shown in Fig. 3d, and the value of *Q* calculated by Eq. (7) was 470.4549 kJ/mol. The value of *Q* was greater than the values of most typical low-alloy and microalloyed steels (270–300 kJ/mol) [13]. Here, *Q* represents the energy of the barrier that the atoms must overcome during hot deformation [14]. Moreover, many studies have demonstrated that high activation energy is generally attributed

to dynamic recovery (DRV) and DRX. Therefore, it can be inferred that the main deformation mechanism of this alloy is either DRV or DRX rather than self-diffusion [10].

The Zener–Holloman (*Z*) parameter, which is a temperature-compensated strain rate parameter, expresses the combined effect of the strain rate and temperature as defined by [15]

$$Z = \dot{\varepsilon} \exp\left(\frac{Q}{RT}\right) = A[\sinh(\alpha\sigma)]^n \qquad (8)$$

Taking the logarithm of both sides of Eq. (8) gives

$$\ln Z = \ln A + n \ln[\sinh(\alpha\sigma)] \qquad (9)$$

The plot of the correlation between ln$Z$ and ln [sinh ($\alpha\sigma$)] is shown in Fig. 4, and the parameters *n* and ln*A* can be obtained as the slope and intercept of the fitted line and are 5.1538 and 42.46492, respectively. The value of *n* is close to the previous value of 5.2129, and 5.2129 is taken as *n* for the subsequent expressions. Accordingly, the hot deformation behavior of MP159 satisfies Eq. (3), and the constitutive equation can be expressed as
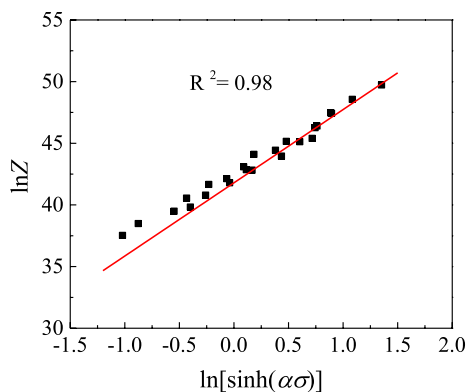
Fig. 4 Plot of the correlation between lnZ and ln[sinh($\alpha\sigma$)]

$$\dot{\varepsilon} = 2.77 \times 10^{18} [\sinh(0.00284\sigma_p)]^{5.2129} \exp\left(\frac{-4704549}{RT}\right) \tag{10}$$

3.3 Processing Maps

A processing map was established to evaluate the hot workability, optimize the processing parameters, and control the microstructures of various alloys during hot deformation. In the dynamic material model (DMM), the specimen under hot working is considered as a power dissipater. The total dissipater power (P) can be divided into two contributions: the power content (G) dissipated by plastic deformation and the power cocontent (J) dissipated in microstructure evolution. Thus, the total power P can be expressed as

$$P = G + J = \int_0^{\dot{\varepsilon}} \sigma d\dot{\varepsilon} + \int_0^{\sigma} \dot{\varepsilon} d\sigma \tag{11}$$

The strain rate sensitivity (m) is the ratio between G and J and is given by

$$m = \frac{dJ}{dG} = \left|\frac{\partial(\ln\sigma)}{\partial(\ln\dot{\varepsilon})}\right|_T \tag{12}$$

The power dissipation efficiency (η) for a nonlinear power dissipater, which reflects the microstructure evolution can be determined as

$$\eta = \frac{J}{J_{max}} = \frac{2m}{2m+1} \tag{13}$$

The power dissipation map is determined by the variation in η with the strain rate and temperature. Generally, the power dissipation map region with a large value indicates sufficient recrystallization and better workability. To determine a suitable processing range, the dimensionless instability parameter $\xi(\dot{\varepsilon})$ based on the principles of irreversible thermodynamics was adopted to identify the unstable region, and the instability criterion is given by

$$\xi(\dot{\varepsilon}) = \frac{\partial\ln(m/(m+1))}{\partial\ln\dot{\varepsilon}} + m < 0 \tag{14}$$

Negative values of $\xi(\dot{\varepsilon})$ represent the instability domains. By superimposing the instability map on the power dissipation map, the processing map can be obtained.

Figure 5 depicts the processing maps at different true strains of 0.2, 0.5 and 0.7 for the alloy. In the processing maps, the shaded area indicates a potentially dangerous deformation regime linked to flow inhomogeneity that gives rise to cracks and that should be avoided. Figure 5a shows that an instability region exists in the temperature range of 920–980 °C and strain rate range of 3.16×10^{-2} to 10 s^{-1} at a strain of 0.2. In the stability region, the peak power dissipation value was approximately 0.39, and this region appeared in the temperature range of 1030–1070 °C and strain rate range of 10^{-2}–3.16×10^{-2} s^{-1}. DRX typically occurs when the efficiency (η) is approximately 0.3–0.5 [16, 17]. This means that DRX occurs at a strain of 0.2 under these hot deformation conditions due to the sufficient energy at high temperatures (1030–1070 °C) and sufficient time at a low strain rate (0.01 s^{-1}). As the strain increased, the deformation instability range moved to moderate temperatures (940–1000 °C) and moderate and high strain rates (1–10 s^{-1}), as shown in Fig. 5b; subsequently, this region
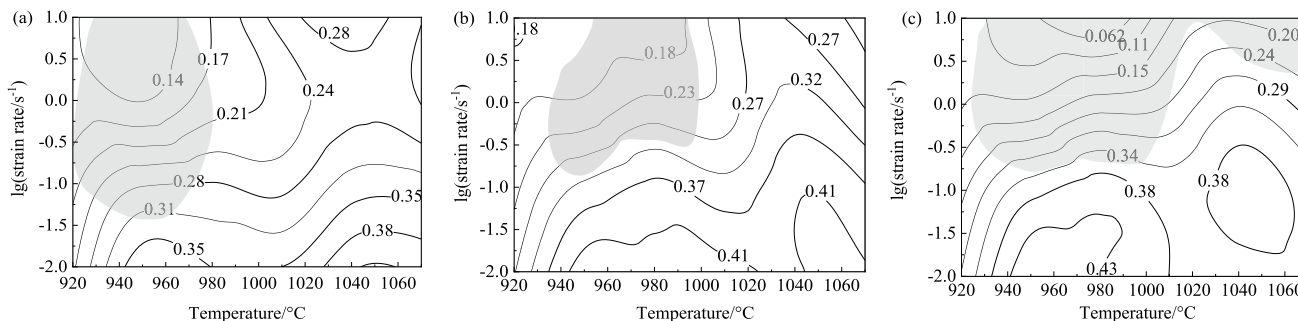

**Fig. 5** Processing maps at different true strains of **a** 0.2, **b** 0.5 and **c** 0.7

expanded to areas with high temperatures and high strain rates, as shown in Fig. 5c. It is concluded that instability domains occurred easily at a high strain rate of 10 s^{-1}, and a strain rate of 10 s^{-1} should be avoided in hot working deformation.

To further analyze the hot deformation behavior of this alloy, the difference between the microstructures of the stability and instability regions was observed. The microstructures of the instability regions are presented in Fig. 6. Figure 6b–d show that full DRX occurred under these deformation conditions, including the instability regions with moderate temperatures and moderate strain rates, as well as the upper shaded area with high strain rates in the processing map. These phenomena may be related to deformation heating [18]. Due to the low thermal conductivity of the MP159 superalloy, the heat generated by plastic deformation could not be released in time at higher strain rates. In addition, Fig. 6b and c show that the DRX grain size increased with increasing strain rate, which was attributed to increased deformation heating. Meanwhile, numerous twins were observed at a high strain rate of 10 s^{-1}, due to the low stacking fault energy of this alloy and the sufficient energy for dislocation movement was provided by the high strain rate. It is seen from Fig. 6a that the MP159 superalloy only occurred partial recrystallization during hot deformation at 950 °C/10 s^{-1}. The deformed grains were elongated perpendicular to the compression direction. The main reason is that the deformation heat is lower at low temperature and moderate strain rate. Deformation heating is harmful for

the mechanical properties and should be avoided in the hot deformation processing of fine-grained MP159 superalloy.

The processing maps demonstrated that the highest power dissipation efficiency was approximately 0.43 and was found in the moderate-temperature and low-strain rate regions (940–980 °C 0.01 s^{-1}). Moreover, in high-temperature and moderate-strain rate region (1040–1070 °C 0.1 s^{-1}), the power dissipation efficiency (η) was approximately 0.38; this value is above 0.35, indicating that DRX may occur for metals with low stacking fault energy [19]. Figure 7 shows the microstructures of the stability regions. In general, a higher power dissipation efficiency indicates a greater availability of energy for microstructure evolution [20]. Fully DRX grains were fine and homogeneous at moderate temperatures and low strain rates with temperatures of 950 and 980 °C and a strain rate of 0.01 s^{-1} (Fig. 7a and b). A higher value of η was observed, and this was considered to be the optimal hot working zone for ensuring better material mechanical properties. DRX occurred at high temperatures and moderate strain rates due to the sufficient energy provided by high temperatures. Nevertheless, the microstructure was uneven and included deformed and grown recrystallized grains (Fig. 7c), and the recrystallized grains showed obvious growth and coarsening (Fig. 7d); thus, neither of these regions is suitable for hot working. The microstructure observations illustrated that the processing map has a good correlation to the microstructure evolution, and optimum processing occurred at deformation temperatures of 940–980 °C and strain rate of 0.01 s^{-1}.

Fig. 6 Microstructures of the instability regions: **a** 950 °C/1 s^{-1}, **b** 950 °C/10 s^{-1}, **c** 980 °C/1 s^{-1} and **d** 1070 °C/10 s^{-1}
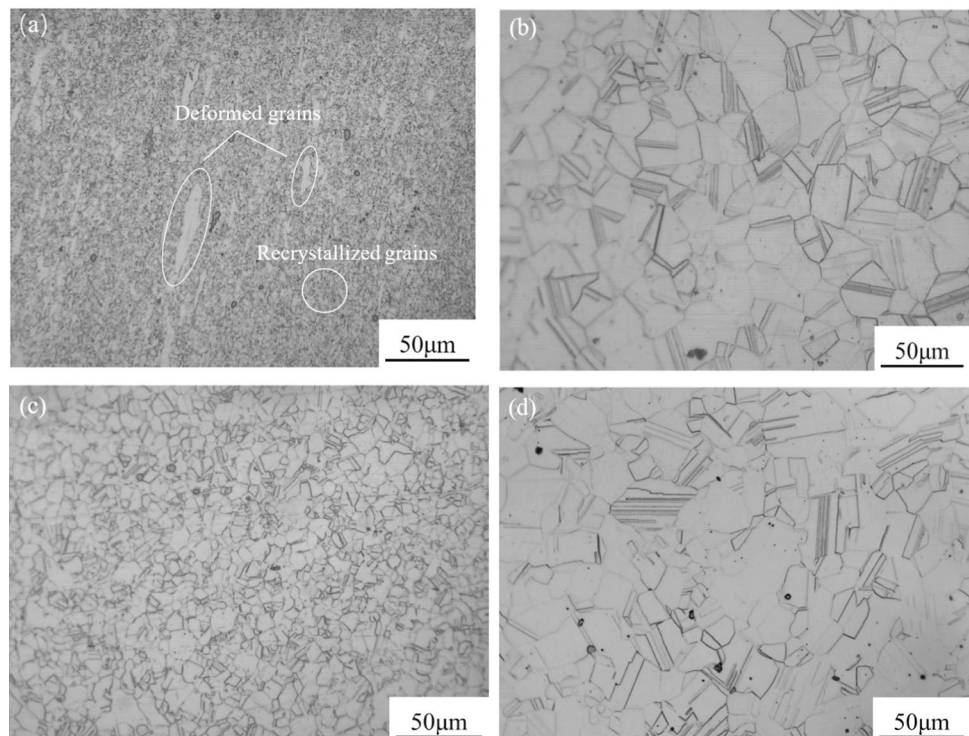
Fig. 7 Microstructures of the stability regions: **a** 950 °C/0.01 s^{-1}, **b** 980 °C/0.01 s^{-1}, **c** 1040 °C/0.1 s^{-1} and **d** 1070 °C/0.1 s^{-1}
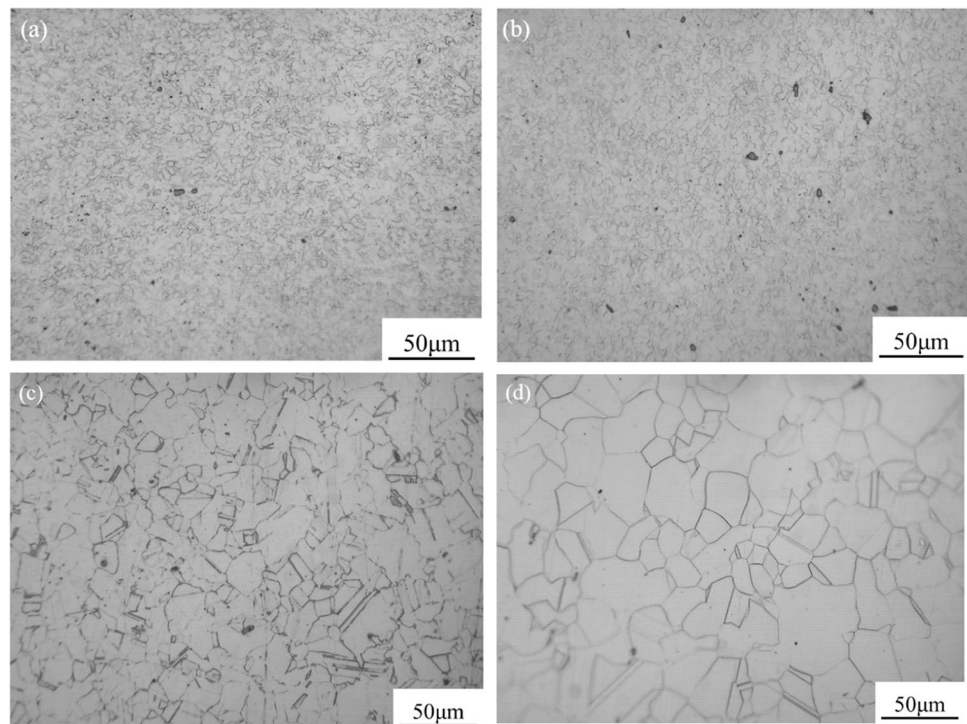
3.4 Effects of Different Deformation Parameters on the DRX Microstructure

3.4.1 True Strain Effects

To evaluate the effects of true strain on the microstructure evolution during hot deformation, the EBSD method was used to characterize the deformed microstructure. The inverse pole figure (IPF) maps and the average misorientation angles of the specimens deformed at 980 °C/0.01 s^{-1} at different strains are provided in Fig. 8. Only a few DRX grains that formed in the original grain boundaries were observed at a strain of 0.3 (Fig. 8a). As the strain increased from 0.7 to 0.9, the volume fraction of the DRX grains increased, as shown in Fig. 8b and c. As the strain increased to 1.3, the DRX grains grew obviously, suggesting that a large true strain can effectively enhance the appearance of DRX. This is attributed to the increasing deformation storage energy and sufficient driving forces for grain boundary motion [21].
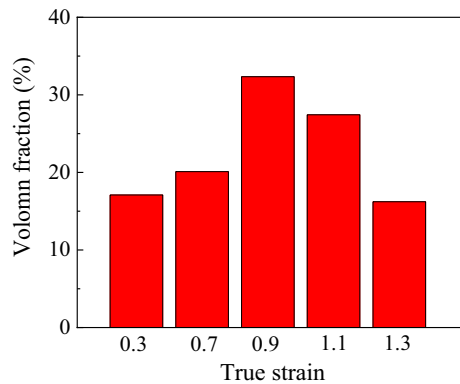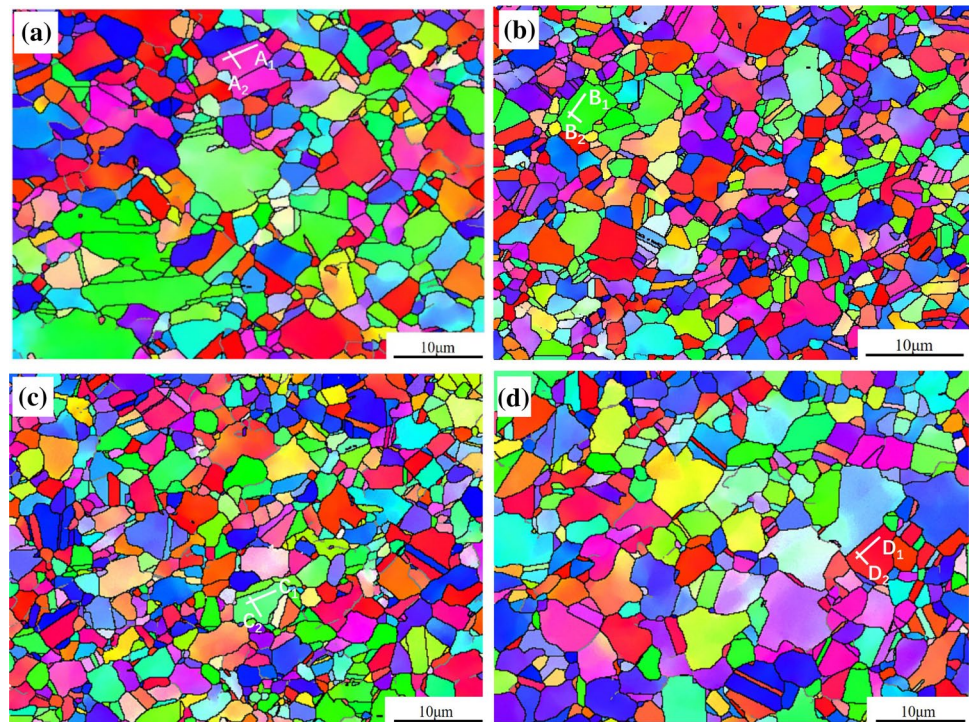
Figure 9 depicts the variation in the volume fraction of low-angle grain boundaries (LAGBs) with true strain for the specimens deformed at 980 °C/0.01 s^{-1}. The increase in the volume fraction of LAGBs from 0.3 to 0.7 is small. At a relatively low deformation strain, the volume fraction of LAGBs first increased slowly with the generation of a few dislocations. As the true strain increased to 0.9, the volume fraction of LAGBs increased rapidly, which can be attributed to the rapid generation of mobile dislocations during this deformation stage. Meanwhile, the deformation storage energy remained relatively low and was insufficient to trigger strong DRX under these deformation conditions. When the strain was between 0.9 and 1.3, DRX with a low dislocation density emerged, resulting in a decrease in the volume fraction of LAGBs.

To further understand the DRX mechanism, the point-to-point misorientations and the point-to-origin misorientations along the lines marked in Fig. 8 are shown in Fig. 10. Both the local and cumulative misorientations within grains and along the grain boundaries did not exceed 5° at all strains, indicating that the subgrain rotation was not distinct. As CDRX mechanism is featured with the progressive rotation of subgrian, these results suggest that CDRX is not occurred in MP159 superalloy deformed at 980 °C/0.01 s^{-1}. Figure 11 provides histograms of the misorientation angle distribution in the range of 0–15° for the specimens deformed at 980 °C/0.01 s^{-1}. The misorientation angles were mostly in the range of 0–10°, while only a few misorientation angles were in the range of 10–15° under all strain conditions. It is well-known that the CDRX mechanism is characterized by progressive subgrain rotation with medium-angle grain boundaries (MAGBs) at angles in the 10–15° range [22, 23]. Thus, CDRX is not the primary DRX mechanism in this study.

Moreover, it is seen from Fig. 8a that some grains with serrated boundaries are observed in the EBSD maps as shown in Fig. 8a. In generally, DDRX features nucleation by bulging grain boundary and followed the growth

Fig. 8 IPF maps and the average misorientation angles of the specimens deformed at 980 °C/0.01 s^{-1} for different strains: **a** 0.3, **b** 0.7, **c** 0.9 and **d** 1.3

Fig. 9 Variation in the volume fraction of LAGBs with true strain for the specimens deformed at 980 °C/0.01 s^{-1}

of recrystallized grains. In order to further characterize the recrystallized microstructure, TEM micrographs of the specimens deformed at different deformation parameters were observed, as depicted in Fig. 12. It is seen from Fig. 12a that a small number of dislocations began to accumulate and multiply, and a heterogeneous dislocation distribution appeared at a relatively small strain stage (strain = 0.3). The local bulging occurred at the initial grain boundary as shown in Fig. 12b, and there is a significant difference in dislocation density on the two sides of the bulging grain boundary. With the strain increased to 0.9 as shown in Fig. 12c, the tangled dislocations will promote the grain boundary bulging. The two sides of

serrated grain boundaries usually retain a high strain gradient, and bulging grain boundaries will be the preferred location for DRX grain nucleation [24, 25]. Figure 12d clearly shows that DRX nucleus located at the bulged grain boundaries, which are the typical characteristics of DDRX nucleate. As the strain further increased to 1.1, as shown in Fig. 12e and f, the microstructure of fully DRX grains nearly free of dislocations was detected, which was ascribed to the elimination of a large number of dislocations during recrystallization nucleation.

The variation of dislocation density in TEM observation is consistent with the quantitative study by the EBSD results. In this present work, the geometrically necessary dislocation (GND) density of the specimen deformed at 980 °C/0.01 s^{-1} with a strain of 0.3, 0.9 and 1.1 is calculated according to Eq. (15) [26]:

$$\rho_{GND} = \frac{2KAM_{ave}}{\mu b} \tag{15}$$

where KAM_{ave} is average value of local misorientation in selected area; b is the Burgers vector, which is 0.25 nm [27]; and μ is the step size. The relationship between the dislocation density and strain was described, as shown in Fig. 13. At the strain of 0.3, the value of dislocation density was 3.95×10^{14}/m^2. With the strain increasing from 0.3 to 0.9, the dislocation density increased from 3.95×10^{14}/m^2 to 5.16×10^{14}/m^2. As the strain further reaches to 1.1, the dislocation density decreased to 4.35×10^{14}/m^2, which
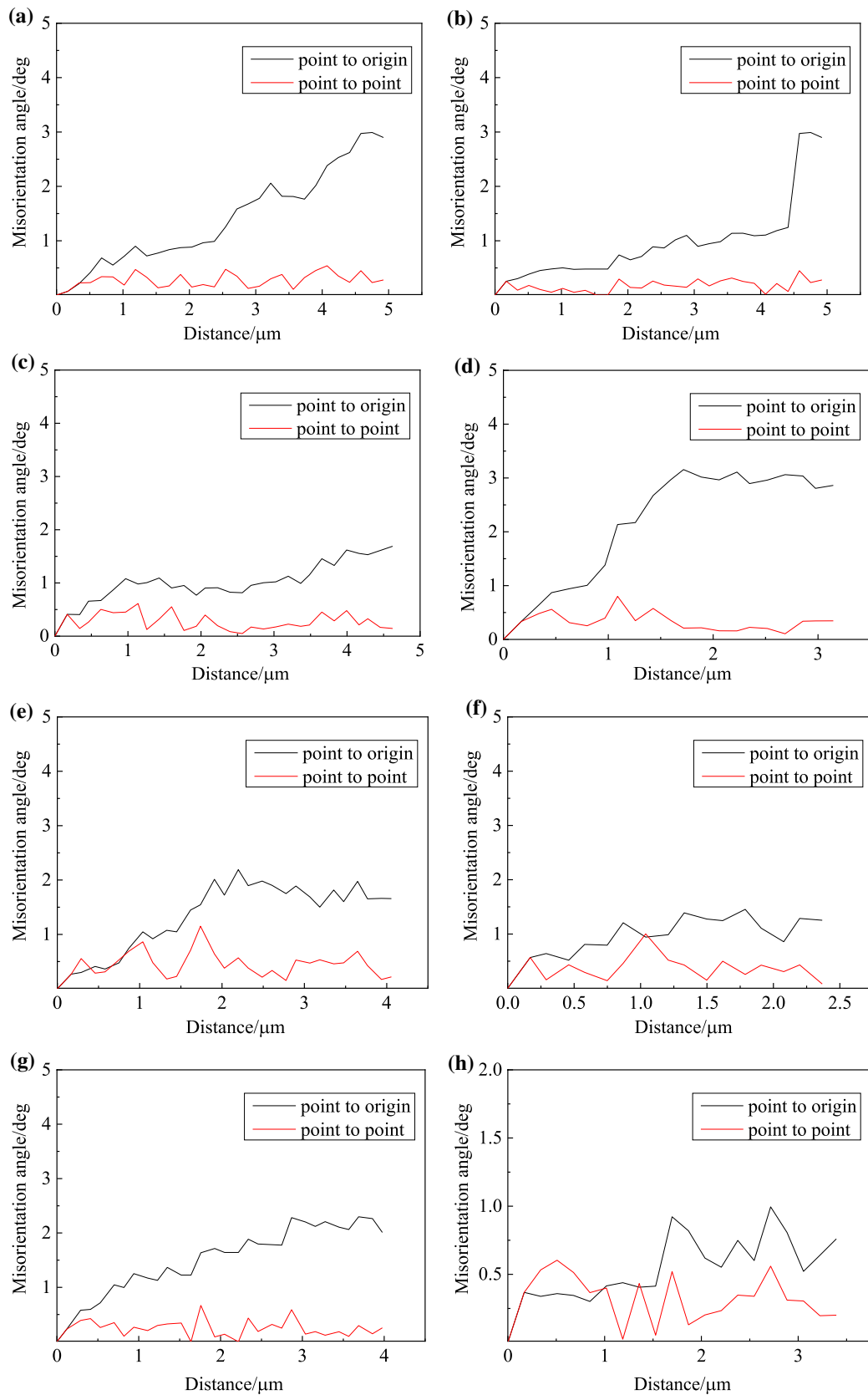
Fig. 10 The point-to-point misorientations and the point-to-origin misorientations along the lines marked in Fig. 8: **a** A_1, **b** A_2, **c** B_1, **d** B_2, **e** C_1, **f** C_2, **g** D_1 and **h** D_2
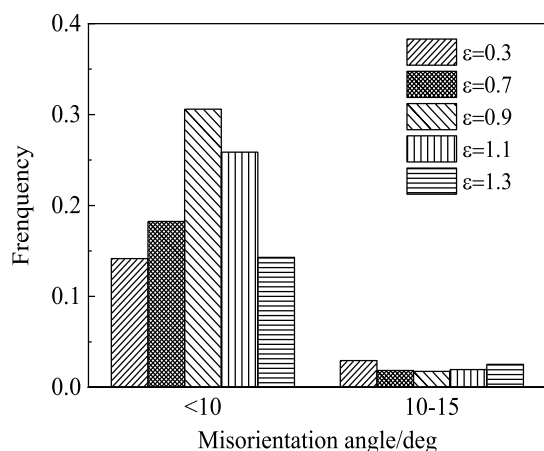
Fig. 11 Histograms of the misorientation angle distribution in the range of 0–15° for the specimens deformed at 980 °C/0.01 s^{-1}

is associated with an increase in the volume fraction of the recrystallized grains.

The TEM observations depict a typical feature of DDRX mechanism, and prove DDRX is the primary DRX mechanism during hot deformation of MP159 superalloy. The schematic map of DDRX nucleation mechanism is illustrated in Fig. 14.

3.4.2 Strain Rate and Temperature Effects

To investigate the effect of the strain rate on the microstructure evolution, the microstructures of the deformed specimens at different strain rates were observed. Figure 15 shows IPF maps of the specimens deformed at a true strain of 1.3 and deformation conditions of 980 °C/0.01–1 s^{-1}. Interestingly, the obvious variation of twins was observed with true strain for the specimens deformed at 980 °C/0.01 s^{-1}, as shown in Fig. 16. The volume fraction of twins boundaries was measured to be 23.6% at a low strain rate of 0.01 s^{-1}. Then the volume fraction of twins boundaries increased from 36.2 to 50.2% with increasing strain rate from 0.1 to 1 s^{-1}. It is well-known that the movable dislocation density depends on the strain rate during thermal deformation, and the relationship can be described as [26, 28]:

$$\dot{\varepsilon} = \boldsymbol{b}\rho\bar{\upsilon} \tag{16}$$

where $\dot{\varepsilon}$ is the imposed strain rate, $\boldsymbol{b}$ is the Burgers vector, ρ is the density of movable dislocation and $\bar{\upsilon}$ is the velocity of dislocation. According to this relationship, the dislocations proliferate rapidly with plastic deformation at high strain

rates. Due to the multiplication and entanglement of numerous dislocations, it is difficult for the dislocations to slip in this alloy with a low stacking fault energy. Twins are easily formed by the so-called growth accident during the migration of the recrystallization front [27–30], which is closely related to the grain boundary migration driving force. At higher strain rates, the frequency of growth accidents is increased and the nucleation of twins is facilitated by the higher stored energy [29, 31], resulting in a large number of twins. Moreover, Fig. 16 shows the recrystallized fraction also increased with increasing strain rate, indicating that recrystallization was sensitive to the strain rate, which could have been attributed to the formation of twins in this alloy. Twins play an important role in the DRX process of alloys with a low stacking fault energy [30, 32]. Twins induce a change in the boundary misorientation and increase the mobility of dislocations, leading to the growth of recrystallized grains with a dislocation-free zone. The twin boundary affects DRX nucleation during hot deformation [3]. The twin boundaries provide positions for DRX nucleation within the grains to promote recrystallization. Thus, twin boundaries may provide a supplementary nucleation mechanism for DRX. For this alloy, as the strain rate increased, more twin boundaries provided nucleation sites for DRX, resulting in an increase in the degree of DRX. In addition, twins lowered the energy required for grain growth and increased grain boundary mobility, which also contributed to the acceleration of the DRX process.

Figure 17 depicts the IPF maps at different deformation temperatures of 950, 980 and 1040 °C for the specimens deformed at 0.01 s^{-1} and a strain of 1.3 and the corresponding average misorientation angles. Many small and refined DRX grains were observed along the grain boundaries at 950 °C. The DRX grains grew with increasing temperature (Fig. 17c), and many coarsened recrystallized grains were observed when the temperature increased to 1040 °C, as illustrated in Fig. 17e. This was attributed to the mobility of the grain boundaries and acceleration of dislocations, and the diffusion rate increased with increasing temperature. Figure 17 also indicates that a higher temperature leads to higher average misorientation angles. The nucleation of DRX grains was induced by dislocation evolution, which is a thermal activation process, and the higher temperature provided a stronger driving force and higher migration speed for boundary migration. Therefore, obvious growth of DRX grains was observed at high temperatures, resulting in an increase in the average misorientation angle from 32.9 and 39.4–to 41.7° (Fig. 17b, d and f).

Fig. 12 TEM micrographs of the specimens deformed at 980 °C/0.01 s^{-1} and different true strains of **a** and **b** 0.3, **c** and **d** 0.9, and **e** and **f** 1.1
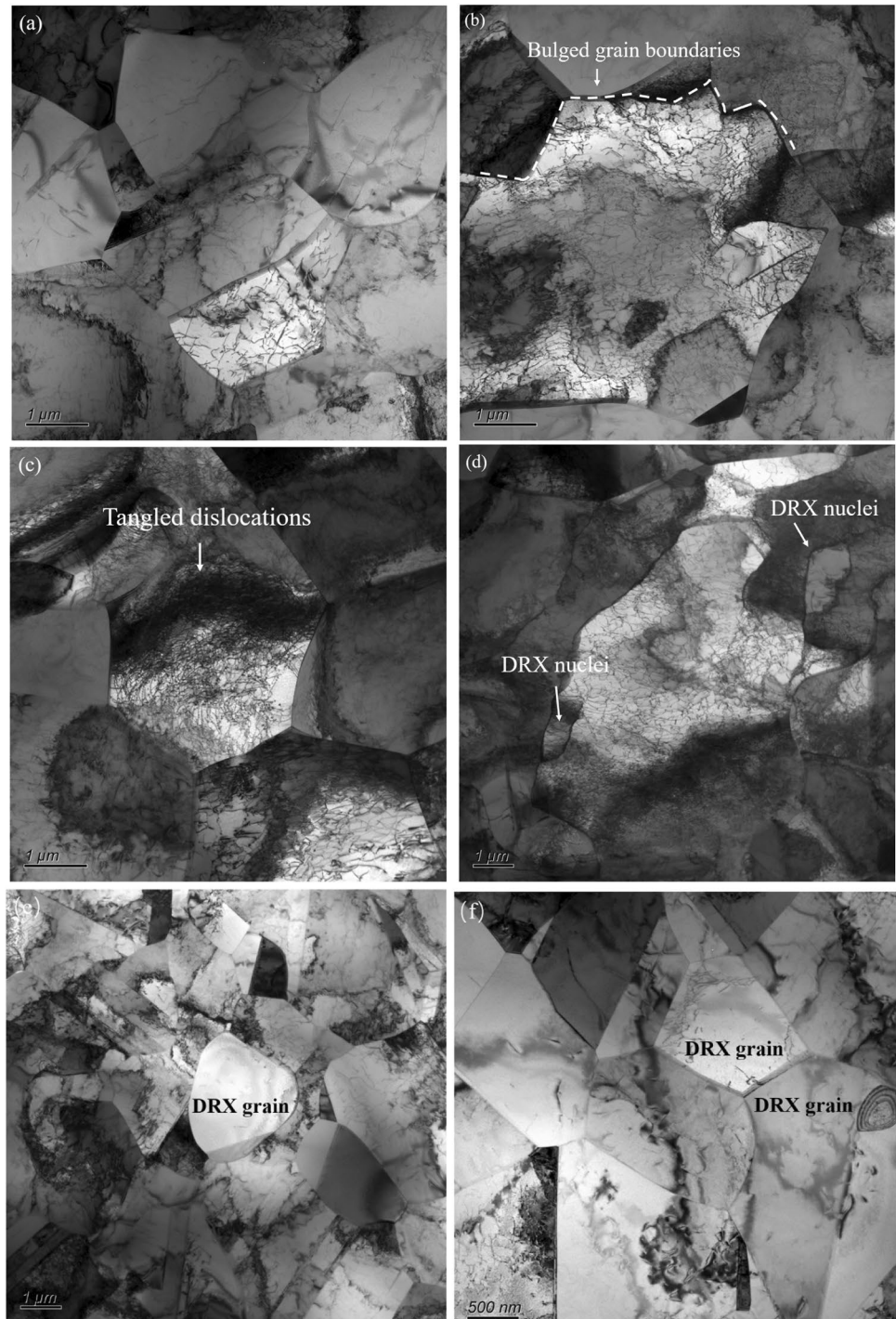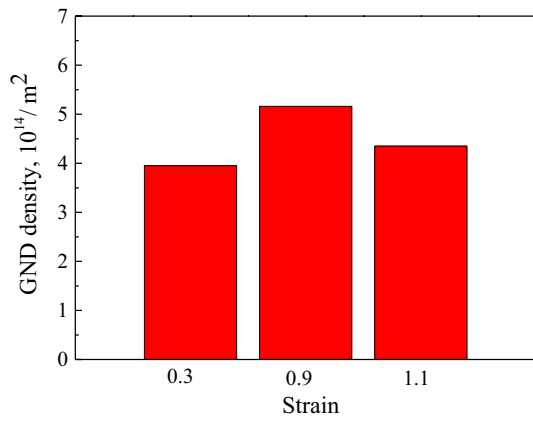
Fig. 13 The density of GND with different true strains

4 Conclusion

Hot deformation tests were conducted in the temperature range of 950–1040 °C and the strain rate range of 0.01–10 s⁻¹. A constitutive model was established, and processing maps were developed based on flow stress curves. The DRX mechanism was revealed. Several conclusions are drawn as follows:

(1) The constitutive equation based on hot deformation at a true strain of 0.7 was established as

$$\dot{\varepsilon} = 2.77 \times 10^{18} [\sinh(0.00284\sigma_p)]^{5.2129} \exp\left(\frac{-4704549}{RT}\right)$$

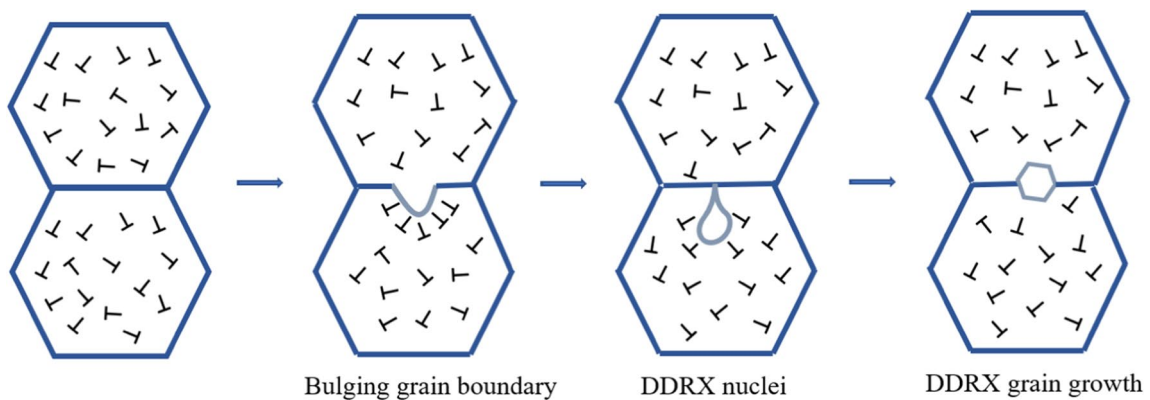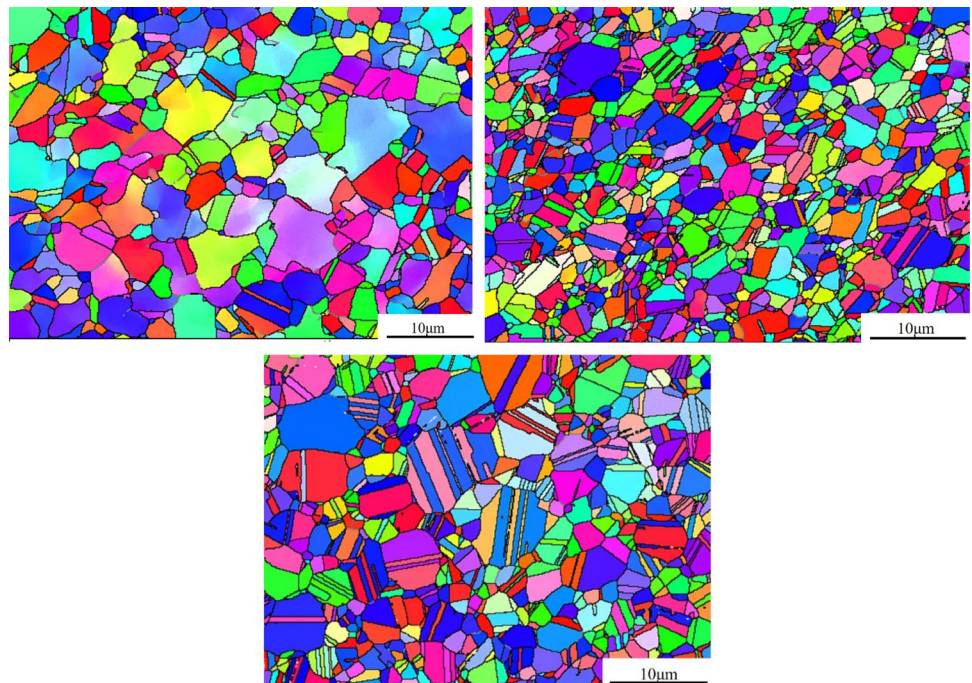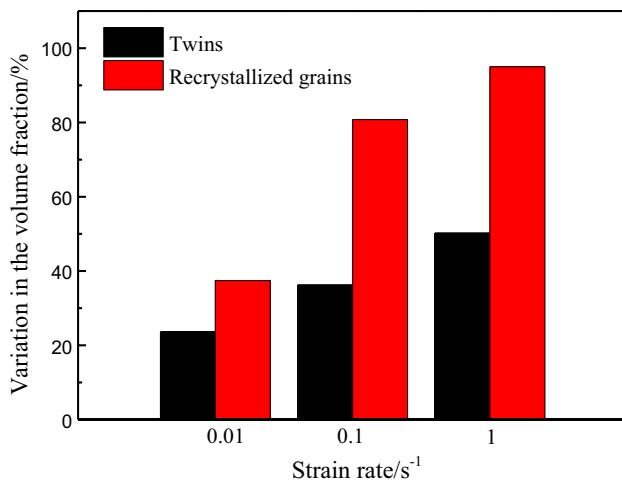Bulging grain boundary   DDRX nuclei   DDRX grain growth

Fig. 14 The schematic map of DDRX nucleation mechanism
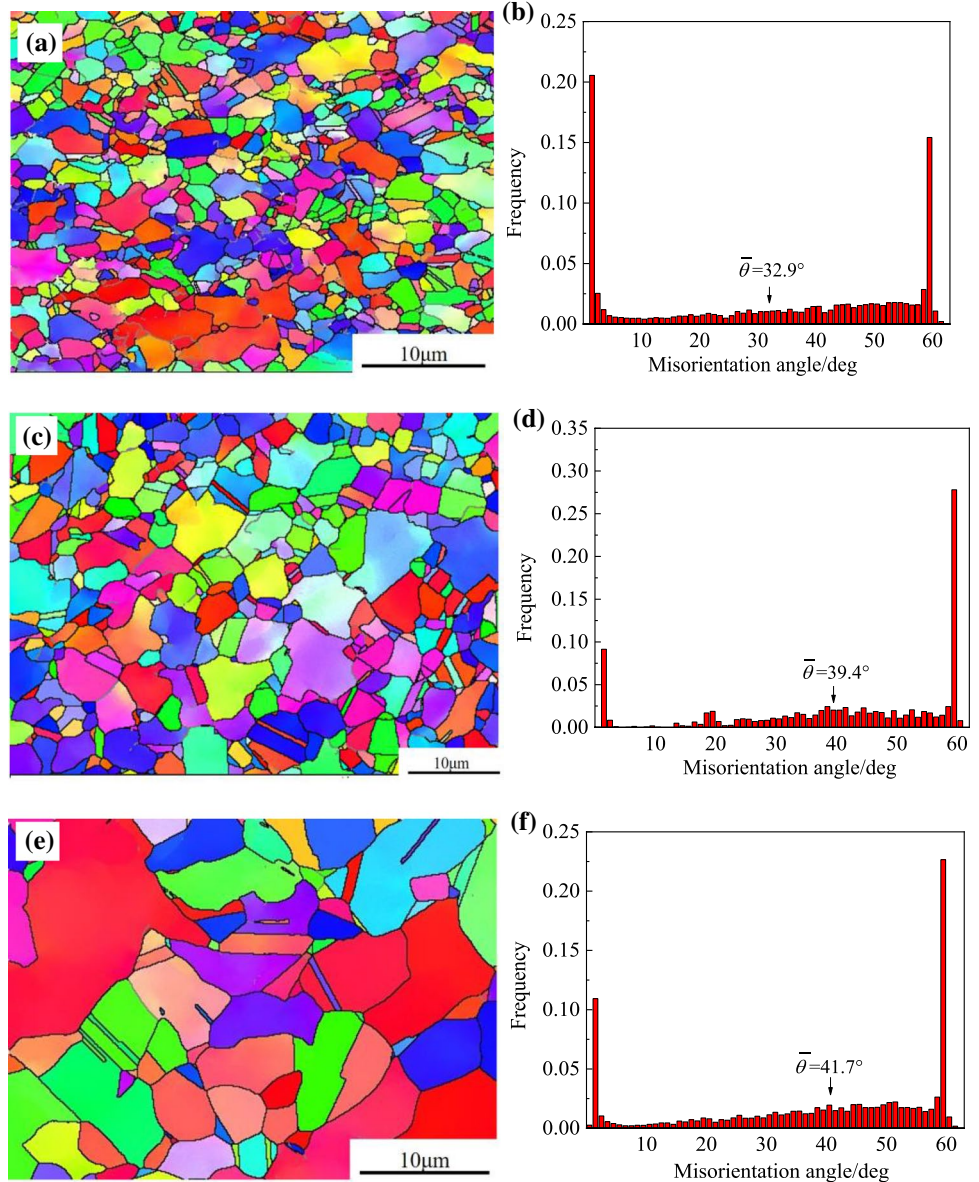
Fig. 15 IPF maps of the specimens deformed at a true strain of 1.3 and deformation conditions of **a** 980 °C/0.01 s⁻¹, **b** 980 °C/0.1 s⁻¹ and **c** 980 °C/1 s⁻¹

Fig. 16 Variation in the volume fraction of twins and recrystallized grains with true strain for the specimens deformed at 980 °C/0.01 s^{-1}

(2) Based on the processing maps and the microstructure observations, the optimal hot work processing regions for the alloy were identified at deformation temperatures of 940–980 °C and strain rate of 0.01 s^{-1}.

(3) The DRX process was sensitive to hot working parameters. The volume fraction of LAGBs for the superalloy deformed at 980 °C/0.01 s^{-1} first increased with increasing strain from 0.3 to 0.9 and then decreased with further increasing strain from 0.9 to 1.3. The volume fraction and grain size of recrystallized grains increased with increasing strain rate and deformation temperature.

(4) A few twins formed at a strain rate of 0.01 s^{-1}. With increasing strain rate from 0.01 to 1 s^{-1}, the volume fraction of twin boundaries increased from 23.6 to 50.2%. The twin boundaries could provide nucleation positions for DRX and accelerate the DRX process.

Fig. 17 IPF maps at different deformation temperatures of **a** 950 °C, **c** 980 °C and **e** 1040 °C for the specimens deformed at 0.01 s^{-1} and a strain of 1.3 and the corresponding average misorientation angles

(5) The DDRX was the primary DRX mechanism for the MP159 alloy during hot deformation.

Declarations

Conflict of interest The authors declare that they have no known competing financial interests or personal relationships that could have appeared to influence the work reported in this paper.

References

1. S. Lu, B. Shang, Z. Luo, R. Wang, F. Zeng, J. Mater. Sci. **34**, 5449 (1999)
2. D.-G. He, Y.C. Lin, J. Chen, D.-D. Chen, J. Huang, Y. Tang, M.-S. Chen, Mater. Design **154**, 51 (2018)
3. M. Azarbarmas, M. Aghaie-Khafri, J.M. Cabrera, J. Calvo, Mater. Sci. Eng. A **678**, 137 (2016)
4. S. Mitsche, C. Sommitsch, D. Huber, M. Stockinger, P. Poelt, Mater. Sci. Eng. A **528**, 3754 (2011)
5. Y. Wu, Z. Liu, X. Qin, C. Wang, L. Zhou, J. Alloy. Compd. **795**, 370 (2019)
6. A.K. Godasu, U. Prakash, S. Mula, J. Alloy. Compd. **844**, 156200 (2020)
7. D.-X. Wen, Y.C. Lin, Y. Zhou, Vacuum **141**, 316 (2017)
8. Y.C. Lin, D.-G. He, M.-S. Chen, X.-M. Chen, C.-Y. Zhao, X. Ma, Z.-L. Long, Mater. Design **97**, 13 (2016)
9. G.W. Han, I.P. Jones, R.E. Smallman, Acta Mater. **51**, 2731 (2003)
10. L.X. Ma, M. Wan, W. Li, J. Shao, X. Bai, J. Alloy. Compd. **808**, 151759 (2019)
11. Y.C. Lin, G.-D. Pang, Y.-Q. Jiang, X.-G. Liu, X.-Y. Zhang, C. Chen, K.-C. Zhou, Vacuum **169**, 108878 (2019)
12. F. Liu, J. Ma, L. Peng, G. Huang, W. Zhang, H. Xie, X. Mi, Materials **13**, 2042 (2020)
13. M. Shaban Ghazani, A. Vajd, B. Mosadeg, Iran. J. Mater. Sci. Eng. **12**, 52 (2015)
14. J.B. Zhang, C.J. Wu, Y.Y. Peng, X.C. Xia, J.A. Li, J. Ding, C. Liu, X.G. Chen, J. Dong, Y.C. Liu, J. Alloy. Compd. **835**, 155195 (2020)
15. C. Zener, J.H. Hollomon, J. Appl. Phys. **15**, 22 (1944)
16. N. Ravichandran, Y.V.R.K. Prasad, Metall. Trans. A **22**, 2339 (1991)
17. N. Srinivasan, Y.V.R.K. Prasad, Mater. Sci. Technol. **8**, 206 (1992)
18. Y.B. Tan, Y.H. Ma, F. Zhao, J. Alloy. Compd. **741**, 85 (2018)
19. Y.V.R.K. Prasad, T. Seshacharyulu, Int. Mater. Rev. **43**, 243 (1998)
20. Y.T. Wu, Y.C. Liu, C. Li, X.C. Xia, Y. Huang, H.J. Li, H.P. Wang, J. Alloy. Compd. **712**, 687 (2017)
21. D. Jia, W.R. Sun, D.S. Xu, F. Liu, J. Mater, Sci. Technol. **35**, 1851 (2019)
22. Y. Wu, H.C. Kou, Z.H. Wu, B. Tang, J.S. Li, J. Alloy. Compd. **749**, 844 (2018)
23. D. Feng, X.M. Zhang, S.D. Liu, Y.L. Deng, Mater. Sci. Eng. A **608**, 63 (2014)
24. Y. Wang, W.Z. Shao, L. Zhen, X.M. Zhang, Mater. Sci. Eng. A **486**, 321 (2008)
25. P. Poelt, C. Sommitsch, S. Mitsche, M. Walter, Mater. Sci. Eng. A **420**, 306 (2006)
26. X.L. Xing, Y.F. Zhou, X. Lu, X.W. Qi, L.J. Zhang, Q.X. Yang, Appl. Surf. Sci. **479**, 634 (2019)
27. Y.H. Zhang, Y. Zhuang, A. Hu, J.J. Kai, C.T. Liu, Scripta Mater. **130**, 96 (2017)
28. Y.C. Lin, F. Wu, Q.-W. Wang, D.-D. Chen, S.K. Singh, Vacuum **151**, 283 (2018)
29. M. Zouari, N. Bozzolo, R.E. Loge, Mater. Sci. Eng. A **655**, 408 (2016)
30. S. Ankem, J.G. Shyue, M.N. Vijayshankar, R.J. Arsenault, Mater. Sci. Eng. A **111**, 51 (1989)
31. Y. Jin, M. Bernacki, G.S. Rohrer, A.D. Rollett, B. Lin, N. Bozzolo, Mater. Sci. Forum. **753**, 113 (2013)
32. Y. Jin, B. Lin, A.D. Rollett, G.S. Rohrer, M. Bernacki, N. Bozzolo, J. Mater. Sci. **50**, 5191 (2015)

Publisher's Note Springer Nature remains neutral with regard to jurisdictional claims in published maps and institutional affiliations.